

# The prediction of vibration, groundborne noise and structure-radiated noise using finite difference methods

R M Thornely-Taylor

*Rupert Taylor Ltd, Uckfield, East Sussex, TN22 3BG, UK*

## Abstract

Application of the finite difference time domain numerical modelling method to the solution of problems in predicting vibration, groundborne noise and noise radiated from vibrating structures, and predicting the performance of vibration-isolating track forms, if sufficient data are available, can closely model the real behaviour of rail systems in three-dimensions in a resource-efficient way can. Detailed representation of structures and lithology to encompass all physical forms of wave propagation is possible, together with methods of addressing frequency-dependent dynamic moduli. Problems associated with arbitrary element shapes can be resolved, together with the topic of boundary absorption. Anisotropic behaviour of soils and other materials is accommodated. Methods of modelling hysteretic, linear viscous and friction damping are available. Combination of the FDTD method with a time-domain boundary element method for predicting radiated airborne noise in the far field allows savings in computing resources. The time-domain approach allows the generation of audio files for the auralisation of results. The problem of gathering reliable and sufficiently detailed information about material properties is significant, particularly with regard to small-strain soil moduli and frequency-dependent loss factors. Results of predictions and measurements of existing railways are presented.

## 1. Introduction

When applied to vibration and groundborne noise from railways, particularly underground railways, the FDTD method [1] facilitates modeling not only of vibration generation by a moving train at the wheel/rail interface, but also of the behaviour of rail support systems, tunnels, structures, soil, buildings and airspaces. Provided that a sufficiently detailed representation of the entire system is included in the model, the accuracy will be dependent on the correctness of the properties assigned to the cells of the model. In practice, the effect of uncertainty in cell properties exceeds the error caused by the discretizing of the wave equation that is the finite difference method.

The finite-difference-time-domain (FDTD) method enables three-dimensional numerical modelling of a system with a moving source to be carried out efficiently. For radiation of noise through air to the far field, the FDTD method can be combined with the boundary element method enabling further computational efficiency.

## 2. The finite difference algorithm

### 2.1 Basic Principles

The wave equation in differential form is as follows

$$\mu \left( \frac{\partial^2 \xi}{\partial x^2} + \frac{\partial^2 \xi}{\partial y^2} + \frac{\partial^2 \xi}{\partial z^2} \right) + (\lambda + \mu) \left( \frac{\partial^2 \xi}{\partial x^2} + \frac{\partial^2 \eta}{\partial x \partial y} + \frac{\partial^2 \zeta}{\partial x \partial z} \right) = \rho \frac{\partial^2 \xi}{\partial t^2} \quad (1)$$

for the  $x$  axis, with corresponding equations for the  $y$  and  $z$  axes, where  $\xi$ ,  $\eta$  and  $\zeta$  are displacements in three orthogonal axes;  $\lambda$  and  $\mu$  are Lamé constants and  $\rho$  is the density. The Lamé constant  $\mu$  is also known as the shear modulus,  $G$ . The Lamé constant  $\lambda$  is also known as the coefficient of dilatation and is given by

$$\lambda = \frac{2\sigma G}{(1 - 2\sigma)} \quad (2)$$

where  $\sigma$  is Poisson's ratio.

The wave equation can be stated in finite difference form by replacing the differential operator with the approximation

$$\frac{\partial \xi}{\partial x} \approx (x[i][j][k] - x[i-1][j][k]) / \Delta x \quad (3)$$

For  $\Delta x \rightarrow 0$  these two forms are identical.

Effectively, the finite difference process is as follows, for each axis,  $i$ ,  $j$  and  $k$ . The example given is for axis  $i$ . Each point  $p(i,j,k)$  lies at the corner of a cell and is assigned a mass equal to one eighth of the sum of the eight contiguous cells as well as a displacement and velocity.

- 1) Compute pressure gradient
- 2) Compute shear force gradient
- 3) Accelerate  $p(i,j,k)$  by  $\Delta v = F / \rho \Delta t$  where  $F$  is the sum of the force derived from stages 1 & 2 and  $\rho$  is the density assigned to the point and  $v$  is the point velocity.
- 4) Displace  $p(i,j,k)$  by  $\Delta x = \Delta v * \Delta t$  where  $x$  is point displacement;  $\Delta t$  is one time step.
- 5) repeat from step 1

The geometric part of wave propagation is completely represented by this process. However, it is not possible to compute force and velocity for the same cell element. Techniques are used to overcome this problem including the use of a staggered grid. For present purposes a process of interpolation to determine force and velocity at the same grid point is preferable, in which the force gradient acting on each of the eight sub-cells is interpolated from the displacement of neighbouring points. Cells are most conveniently rectangular, but other shapes are possible [2][3].

In principle the entire system can be represented by appropriate coding of cells to represent the vehicle body, suspension, bogies, wheels etc.

The FDTD algorithm can be written in terms of velocity only, discarding displacement, but this is only convenient for an infinite, homogeneous, isotropic medium.

## 2.2 Basic Principles

Because of the general nature of the wave equation, provided that cells are coded appropriately, all wave types will emerge in an FDTD model provided that the wavelength is several times the individual cell size. Thus compression waves, shear waves, Rayleigh waves where there is a surface between the ground and an airspace or void, Stoneley waves at interfaces and Lamb waves in layers all occur where relevant without additional coding. In beams and plates, bending waves occur automatically and appropriate representation of supports produces correct beam and plate modes.

### 2.3 Damping

Damping can take several forms, including viscous, friction and hysteretic damping. In the finite difference algorithm it is possible to create a frequency dependent (including a frequency-independent) damping term with any desired spectrum shape using the relaxation principle of Boltzmann [4] such that

$$s(t) = D_1 \varepsilon(t) - \int \varepsilon(t - \Delta t) \varphi(\Delta t) d(\Delta t) \quad (4)$$

where  $\varphi(\Delta t) = \frac{D_2}{\tau} e^{-\Delta t/\tau}$  is an after-effect function,  $D_2$  is a constant and  $\tau$  is a relaxation time.  $D_1$  is a modulus,  $s(t)$  is stress and  $\varepsilon(t)$  is strain. By combining several after-effect functions with different values of  $D_2$  and  $\tau$ , any relationship between loss factor and frequency may be represented. Note that in the frequency domain the integral has a real and imaginary part, with the result that the value of the  $D_1$  modulus is reduced by the inclusion of the relaxation terms. Depending on the choice of the constants and relaxation times, the stiffness of a resilient element will be frequency-dependent, and the value of  $D_1$  must be adjusted at the same time that  $D_2$  and  $\tau$  are selected to give the required dynamic stiffness. Equation (4) can be discretized and combined with the finite difference algorithm for the wave equation.

### 2.4 Model boundaries

The potential problem of reflections from model boundaries can be overcome by the use of an impedance matching technique. This effectively assigns to the cells which are required to be non-reflective on the boundaries of the model the properties of a massless viscous damper such that

$$\frac{\eta K''}{\omega} = - \left( \rho c + \frac{D(\xi_0 - \xi_{-1})}{\rho \Delta x v_0} \Delta t \right) \quad (5)$$

where  $\eta$  is the loss factor (dimensionless),  $K''$  is the imaginary part of a complex spring stiffness in which the real part is zero,  $\omega$  is the angular frequency,  $\rho c$  is the characteristic impedance of the medium,  $\xi_0$  and  $\xi_{-1}$  are the displacements of cell points 0 and -1 where the boundary is at cell 0,  $\rho$  is the density of the cell contents and  $v_0$  is the velocity of cell 0.

### 2.5 Porous media and water saturation

The topic of sound propagation in fluid-saturated porous solids was pioneered by Biot [5][6], Biot predicted the existence of two compressional waves and one shear wave. One of the compressional waves attenuates very rapidly, and the other can be regarded as a modified form of the compressional wave which would exist in the dry solid.

Biot's work was developed by Stoll [7] to include friction damping in the frame moduli. The FDTD implementation of the Biot-Stoll equation can be simply achieved by using the equation to compute compressional wave speeds of the first kind, and shear wave speeds, and the frequency-dependent loss factor, and adjusting the parameters of the cells to yield the appropriate wave speeds and loss factors. Because the compressional wave of the second kind attenuates very rapidly, it can be ignored. However, it does carry part of the vibrational energy, and at reflections between interfaces, for example at the top of a water table, some reflected energy will appear as a compressional wave of the second kind, to be rapidly attenuated. This is a form of damping which is not otherwise represented and may partially account for the higher observed attenuation rates than can be accounted for mathematically.

## 2.6 Anisotropy

Many soils, particularly overconsolidated clays, have moduli which depend on direction. A particular advantage of the FDTD method is that difference values of  $G$  and  $D$  can be applied to the  $i$ ,  $j$  and  $k$  directions. The dependence of moduli on confining pressure, and thereby on depth below ground can also be taken into account by varying the values of  $G$  and  $D$  with increasing depth.

## 2.7 Stability

For a FDTD model to be stable, the time step used must not exceed the Courant number, given by

$$\Delta t \leq \frac{1}{c \sqrt{\frac{1}{\Delta x^2} + \frac{1}{\Delta y^2} + \frac{1}{\Delta z^2}}} \quad (6)$$

where  $\Delta x$ ,  $\Delta y$ , and  $\Delta z$  are the cell sizes in the  $i$ ,  $j$  and  $k$  directions.

## 2.8 Bandwidth

The lower limit of the bandwidth of an FDTD model is dependent on the run time, which should preferably be at least  $4/f_0$  where  $f_0$  is the lower boundary of the frequency range. The upper limit is defined by the cell size, and the must be at least two cells per wavelength, and preferably four or more cells per wavelength. The input forcing signal should be filtered with a cut-off at the upper frequency limit of the bandwidth.

## 2.9 Excitation and input force

For a railway model, the excitation is, firstly, a time-dependent force caused by the wheel/rail roughness profile. This is input as the force caused by the displacement of the Hertzian contact spring between a railway wheel and the rail, typically assumed to be 1.2 GN/m. However, the train is moving, so the point of contact must move at the same rate. To avoid a step-wise motion, the application of the force to the rail is preferably achieved by polynomial interpolation across the edges of adjacent cells. Secondly, the effect of the moving load at the wheel is modelled by applying the acceleration due to gravity to the wheel at each time step.

The wheel/rail roughness profile may be an actual profile measured from actual track, or a synthesised profile which has the amplitude and spectrum shape typically found on the type of railway in question. Joints in the rail or flat spots on the wheel tread can be introduced as superimposed displacements in the roughness signal.

## 2.10 Output

Primary output is the displacement or velocity of cells of interest, in the time domain. This may be converted to audio format (e.g. WAV) to enable the modelled signal to be auralised. The time domain signal is normally subjected to a frequency transform and expressed as a 1/3 octave spectrum. The velocity and pressure at cells of the boundary of a radiating object may be used in a boundary element algorithm within the FDTD code [1] for predicting, for example, airborne sound levels at distances outside the extent of the FDTD grid.

### 3. Choosing Cell Properties

The accuracy of an FDTD model depends, of course, on the appropriate assignment of properties to each cell. The properties to be assigned are shear modulus, compression modulus, (or shear modulus and Poisson's ratio), loss factor and density. Loss factor is likely to be frequency dependent, and the use of the Boltzmann relaxation method produces some frequency dependence in the moduli, with the result that the Boltzmann parameters must be chosen not only to give the appropriate loss factor, but also the appropriate shear and compression moduli all as a function of frequency.

Because of the limitations of the Courant number, very small cell sizes, for example to represent the webs and flanges of steel beams, can lead to excessively short timesteps and excessive run times. This problem can be overcome by representing an element such as an "H" section beam as a rectangular bar, and assigning sizes for  $\Delta x$ ,  $\Delta y$  and  $\Delta z$ , and for shear and compression modulus, to give the same value of bending stiffness in each direction, and mass per unit length, as those possessed by the actual section. Bending stiffness is the product of Young's modulus and the second moment of area of the section. This simplification is acceptable when the only significant contribution of the element is in terms of bending waves. In cases where longitudinal wave propagation along the beam is significant, its true moduli and cross section must be used.

For concrete structures, a decision has to be made on whether to assume the long-term or short-term Young's modulus, and the normal approach is to assume short-term values.

For soils and rocks, moduli for infinitesimally small strains must be used, which effectively means that data from measurements of wave speeds, rather than from direct measurements of moduli are required, and these must be adjusted for the effect of confining pressure, and depth below ground. Where appropriate anisotropic material such as clay may require different moduli for each direction. The presence of a water table must be taken into account by using appropriate saturated and unsaturated values for  $D$ .

When a model includes an airspace, for example air in a room, and sound pressure levels are to be computed, the effect of sound absorption in the room must be taken into account. This can be simplified if the reverberation time of the room is known or can be reliably assumed, and the effect of absorbent room surfaces taken into account by artificially increasing air absorption, giving air a loss factor of

$$\eta \approx \frac{4.4}{f T_{60}} \quad (7)$$

where  $f$  is frequency in Hz.

### 4. Model Validation

To test the ability of the FDTD method to give useful predictions of groundborne noise and vibration for a typical underground railway (using readily available assumptions) a proprietary implementation, *FINDWAVE*<sup>®</sup> was used to model 3-axis vibration of the ground surface above an operating light railway in twin bored tunnels in layered ground. The results were compared with measurements.

The largest uncertainty attaching to any case of groundborne noise is the roughness profile of the train vehicle wheels and of the rails. In order to reduce the uncertainty from this cause, measurements of the actual rail roughness, and indirect determination of the wheel roughness, were made.

Figure 1 shows a longitudinal section through the tunnels. The measurement location was in the middle of an open car parking area selected to be equidistant from each tunnel.

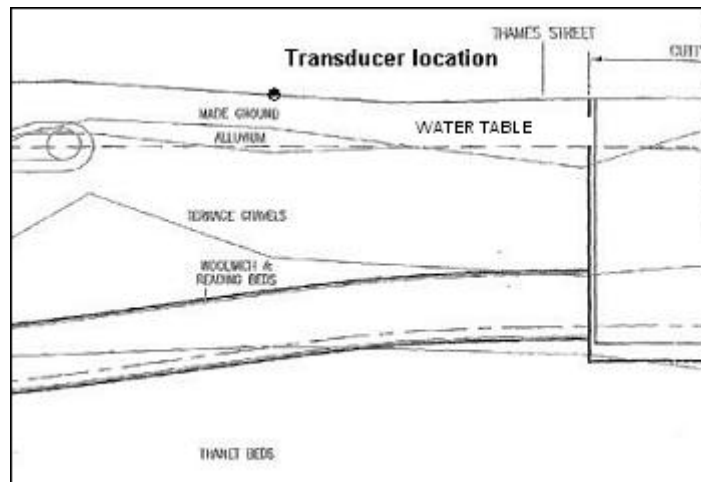


Figure 1 Longitudinal section through validation site

#### 4.1 Measurement procedure

Two measurement exercises were carried out: (i) measurements of rail roughness and (ii) measurements of three-axis ground surface vibration. Rail vehicle wheel roughness was deduced by the method set out in the Appendix.

For the vibration measurements, three axes were measured, namely vertical, lateral and longitudinal (parallel with the tunnel centreline).

Passes of a single vehicle pair, one pass in each tunnel, that did not appear to have noticeable wheel defects were selected for use in the validation exercise. The procedure set out in the Appendix to deduce wheel roughness indicated that in a few 1/3 octave bands it was a significant contributor relative to rail roughness. Figure 2 shows the wheel and rail roughness for the sections of tunnel represented in the model.

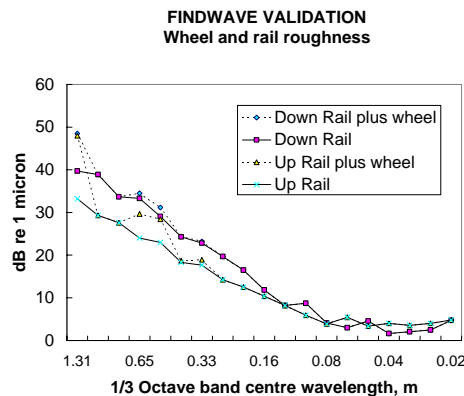


Figure 2 Measured and indirectly determined rail and wheel roughness

Note: The wavelengths correspond to standard frequency bands for the modelled train speed of 47 km/h

Rail roughness was measured at intervals of approximately 0.25mm. Lengths of 65m relevant to the location of the rail vehicles during the measurements were extracted and subjected to frequency transform by a series of eight overlapped 1/3 octave spectra each approximately 16m

long. These were presented as frequency spectra for the relevant train speed directly beneath the measurement location, (47 km/h) and the logarithmic mean of the eight spectra was used.

## 5. The prediction model

A matrix of 108 x 124 x 140 cells each .25m (vertical) x .25m (lateral) x .217m (longitudinal) was generated as illustrated in figure 3 . The properties assigned to each cell were as shown in table 1. Where the cell size differs from the actual feature, i.e. the rail cross section which is less than .25m x .25m, the moduli and densities are reduced to give the correct bending stiffness and mass per unit length. The cells representing baseplates were given moduli that gave the correct vertical dynamic stiffness.

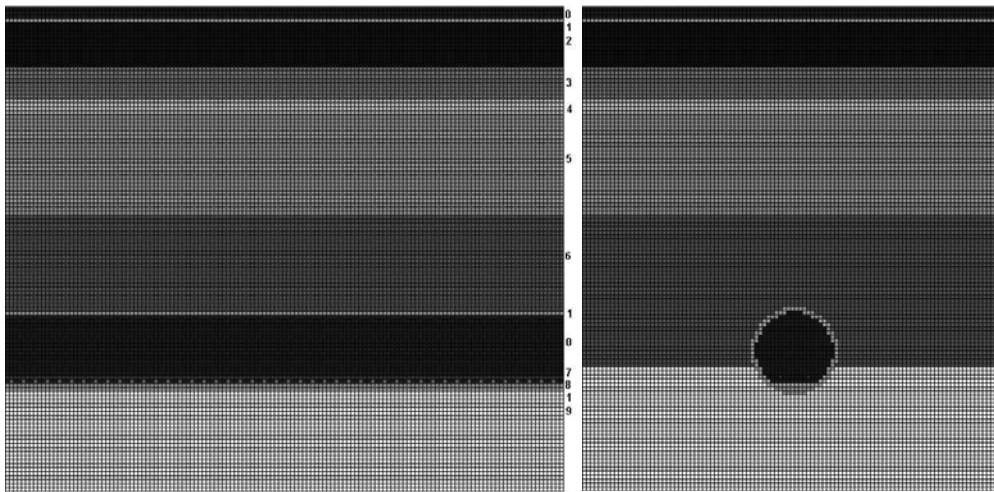


Figure 3 Sections through model (left: longitudinal; right: transverse)

The model was connected end-to-end to limit the length and avoid an excessive run time. This effectively models an infinitely long train, and may be expected to lead to some overprediction. The lateral boundaries and the bottom boundary were made non-reflecting. The model was run for 32768 time steps for a total of 1 second.

## 6. Input data

The train consists of two three-bogie articulated vehicles coupled together. The speed was 47 km/h. The model input data were as shown in table 1:

Length over couplers (each vehicle)	28.8	m
Vehicle mass per wheel	3249	kg
Vehicle secondary suspension stiffness	383	kN/m
Secondary suspension damping	37.5	kNs/m
Sprung mass of bogie per wheel	859.5	kg
Stiffness of primary suspension	1.14	mN/m
Primary suspension damping	1.6	kNs/m
Unsprung mass per wheel	468	kg
Hertzian contact stiffness	1.2	GN/m
1 <sup>st</sup> axle distance from body end	3.05	m
2 <sup>nd</sup> axle distance from body end	4.95	m
3 <sup>rd</sup> axle distance from body end	13.05	m
4 <sup>th</sup> axle distance from body end	14.95	m
5 <sup>th</sup> axle distance from body end	23.05	m

Table 1 Vehicle properties

The track consisted of BS 80A rail support on resilient baseplates, having a cast top plate on a cellular polymer pad through which protrude spring-loaded holding down bolts. The baseplates were fastened to a concrete invert. The tunnel is 5.25m internal diameter with segmental concrete linings 250mm thick.

The dynamic stiffness of the baseplate pad was stated as 10MN/m at 40 Hz by the manufacturers, and the loss factor,  $\eta$ , was assumed to be 0.1.

The soil properties were as shown in table 2 in terms of wave speeds. Soil properties were selected based on their characteristics and published data for comparable soils. As far as loss factor is concerned, neither the Biot-Stoll equation for propagation in water-saturated porous media, nor soil non-linearity can account for a value for  $\eta$  of more than about 0.03-0.05 except at high frequencies in saturated ground.

	Item	$\mu$ (GPa)	$\lambda$ (GPa)	$\rho$ (kg/m <sup>3</sup> )	$\eta$ (dimensionless)
0	Air	0	13.96	1.18	0.001
1	Concrete	20.8	4.25	2400	0.01
2	Made Ground	0.067881	0.33	1500	0.05
3	Alluvium	0.067881	0.33	1500	0.05
4	Terrace Gravels	0.2701	0.33	2000	0.05
5	Saturated Terrace Gravels	0.2835	0.47	2100	0.05
6	Lambeth Group	0.5804	4.53	2100	0.05
7	Baseplates	0.0154	0.22	100	0.1
8	Rail	3.511	0.29	776.59	0.05
9	Saturated Thanet Beds	0.4417	0.32	2100	0.05

Table 2 Soil properties: key to the codes in Figure 3

\*adjusted to give bending stiffness and mass per unit length appropriate to rail section

†adjusted to give dynamic vertical stiffness of 10 MN/n.

The loss factors shown in table 2 are represented in the model as frequency-dependent in the manner shown in Figure 4.

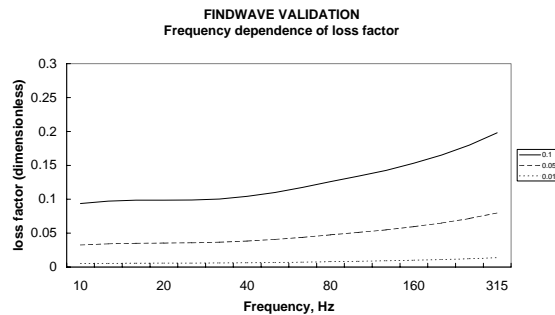


Figure 4. Frequency dependence of loss factors.

## 7. Results

Two model runs were carried out, the first with zero rail roughness and the second with a standardised rail roughness profile. The results demonstrated that in this case the ground surface vibration is primarily influenced by roughness and that gravitational effects were of second order. The results were therefore subsequently adjusted to the measured rail roughness for the

northbound and the southbound tunnels, corrected for wheel roughness using the method set out in the Appendix.

The model results together with the measured results are plotted in figures 5 to 8 in terms of 1/3 octave band 3-axis velocity in dB re 1 nanometre per second.

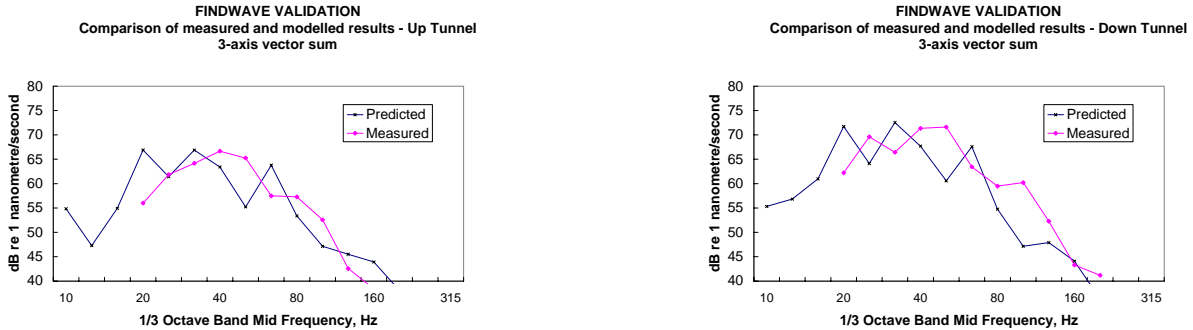


Figure 5 Measured and modelled results (vector sum) for Up tunnel (left) and Down tunnel (right)

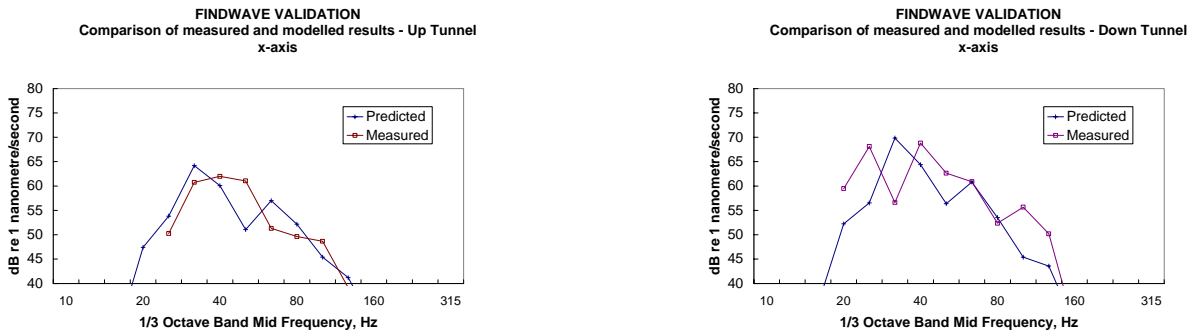


Figure 6 Measured and modelled results (lateral) for Up tunnel (left) and Down tunnel (right)

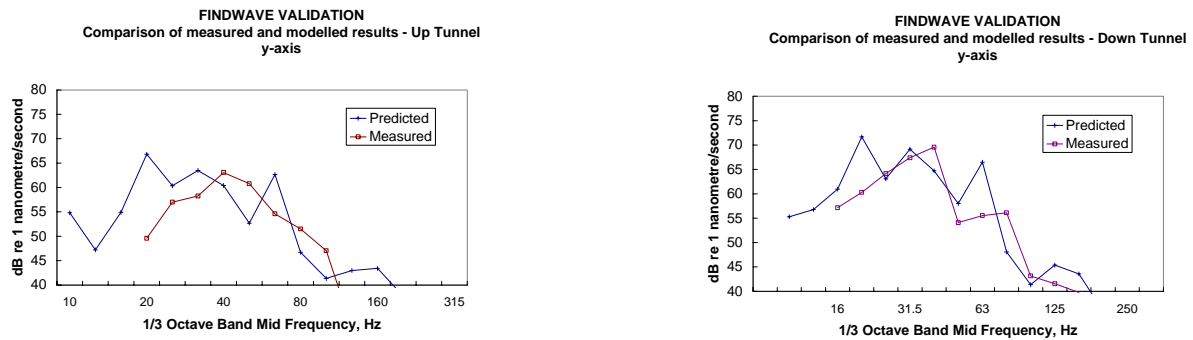


Figure 7 Measured and modelled results (vertical) for Up tunnel (left) and Down tunnel (right)

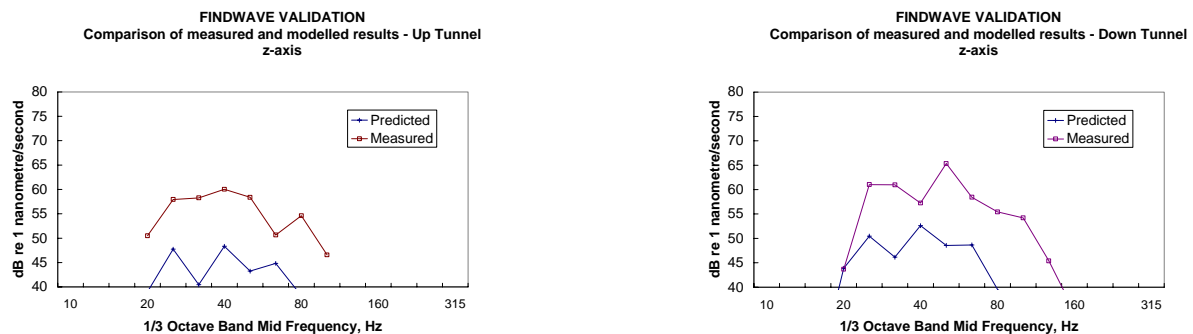


Figure 8 Measured and modelled results (longitudinal) for Up tunnel (left) and Down tunnel (right)

## 8. Discussion

Figure 5 shows broadly similar spectrum shapes for the predicted and modelled results, although secondary peaks in the 1/3 octave band spectrum do not coincide precisely. The same is true of the results for the  $x$ - (lateral) and  $y$ - (vertical) axes in figures 6 and 7. There is poor agreement for the  $z$ - (longitudinal) axis in figure 8 due to the fact that the model is connected end-to-end and is therefore for an infinitely long train, whereas the actual train is only 57.6m long.

In terms of A-weighted overall noise level, the measured and modelled results differ by only 0.3 dB(A) for the Down tunnel, but there is an underprediction of 3 dB(A) for the Up tunnel.

## 9. Conclusion

The FDTD method, when applied to a practical case for which broad assumptions about ground conditions are made, gives predictions that correspond reasonably well with measured data. The largest area of uncertainty is wheel/rail roughness, and when using the prediction method for an unbuilt railway use of maximum roughness amplitudes forming part of a railway maintenance policy enables a limit to be applied to the range on uncertainty from this cause.

### Appendix: Indirect determination of wheel roughness

It can be assumed that there are two independent, linear sources: rail roughness and wheel roughness, both located at the wheel/rail interface.

The mean square measured overall vibration velocity on the ground surface, in any frequency band, will be the sum of the mean square vibration velocity caused by the rail (R) in the relevant tunnel and the mean square vibration velocity caused by the wheel (W) of a particular vehicle.

The surface mean square vibration velocity (M) is determined by measurement, so for a pair of train passages of the same vehicle in tunnel 1 and tunnel 2, at a location midway between the two tunnels where the propagation conditions can be assumed to be the same:

$$M_1=R_1+W; M_2=R_2+W \quad (8)$$

While the values of  $R_1$  and  $R_2$  are unknown, the ratio of  $R_2$  to  $R_1$  will be the same as the ratio of the source rail roughness in tunnel 2 and tunnel 1 (which have been measured), so, putting  $k=R_2/R_1$  gives

$$W=(M_2-kM_1)/(1-k) \quad (9)$$

Thus the wheel roughness of a vehicle can be obtained from measurements of the same vehicle in the northbound and southbound tunnels at the same speed, at a location midway between the tunnels where the propagation conditions can be assumed to be the same for both tunnels. There will be some error due to inequalities of the speed profile and differences in ground conditions for the two tunnels. The magnitude of the error can be estimated from the variation in the value of  $R_2$  and  $R_1$  (which should be constant) obtained for different measurement pairs.

## Acknowledgement

The validation work was funded by Central London Rail Links Ltd, for whom the rail roughness measurements were made by AEA Technology.

The FDTD modeling package *FINDWAVE*<sup>®</sup> is owned by the author.

## References

---

- 1 R.M.Thornely-Taylor . The prediction of vibration, ground-borne and structure-radiated noise from railways using finite difference method- Part1- theory. Proceeding of the Institute of Acoustics. Vol.26. Pt.2 2004. pp 69-79.
- 2 D. Botteldooren, Acoustical finite-difference time-domain simulation in a quasi-Cartesian grid, J. Acoustic.Soc. Am. 95(5) Pt 1, May 1994.
- 3 J.G. Tolan, and J.B. Schneider, Locally conformal method for acoustic finite-difference time-domain modeling of rigid surfaces, J. Acoustic. Soc. Am. 114 (5) November 2003
- 4 L. Boltzmann. Ann. Physik, Erg. Bd. 7 (1876) 624-654
- 5 M.A. Biot, Theory of Propagation of Elastic Waves in a Fluid-Saturated Porous Solid – I Low Frequency Range Frequency Range, J. Acoust. Soc. Am. 28, 2 1956
- 6 M.A. Biot, Theory of Propagation of Elastic Waves in a Fluid-Saturated Porous Solid – II Higher Frequency Range, J. Acoust. Soc. Am. 28, 2 1956
- 7 R.D. Stoll, Marine Sediment Acoustics, J. Acoust. Soc. Am 77 (5) May 1985